Electrochimica Acta 389 (2021) 138563

Contents lists available at ScienceDirect

Electrochimica Acta

journal homepage: www.elsevier.com/locate/electacta

Transport of secondary carriers in a solid lithium-ion conductor

Guanchen Li[a,b], Charles W. Monroe[a,b,*]

[a] Department of Engineering Science, University of Oxford, Oxford OX1 3PJ, United Kingdom
[b] The Faraday Institution, Harwell Campus, Didcot OX11 0RA, United Kingdom

ARTICLE INFO

Article history:
Received 29 March 2021
Revised 23 April 2021
Accepted 3 May 2021
Available online 7 May 2021

Keywords:
multi-ion transport
oxide garnet solid electrolyte
superionic conductor
solid-state lithium battery
dopants

ABSTRACT

Inorganic-solid lithium electrolytes are typically thought of as single-ion conductors, but the presence of secondary carriers can strongly affect their performance. Conventional descriptions of multi-carrier transport neglect both interactions between mobile species and stress diffusion — phenomena which can markedly impact the electrical response. We apply irreversible thermodynamics to develop a chemo-mechanical transport model for elastic-solid ionic conductors containing two mobile ions. We simulate lithium-ion conducting $Li_5La_3Nb_2O_{12}$ (LLNO) garnet oxide, a material within which experiments have shown that mobile protons can be freely substituted for lithium to form $Li_{5(1-y)}H_{5y}La_3Nb_2O_{12}$. When subjected to a current, we find that proton-substituted LLNO exhibits bulk lithium polarization, whose extent is partially controlled by cation/cation interactions. Secondary carriers segregate naturally if their global concentration is low, accumulating in a thin boundary layer near the cathode. We quantify the limiting current and Sand's time, and analyze experimental data to show how competitive proton transport affects LLNO performance.

© 2021 The Authors. Published by Elsevier Ltd.
This is an open access article under the CC BY license (http://creativecommons.org/licenses/by/4.0/)

More conductive, durable electrolyte materials would enable higher-power, safer energy storage systems. Solid electrolytes have promising mechanical properties, but are generally less conductive than liquids and can be prone to chemical instability [1] and dendrites [2]. In solid lithium-ion conductors, dopants have been exploited to enhance ionic conductivity and chemical stability [3,4], while impurities [5] and defects [6] have been observed to facilitate material degradation.

Unlike liquid electrolytes, solid ion conductors do not readily accommodate the volume changes that typically accompany ion-concentration polarization. Because squeezing or stretching tough sublattices produces large stress, the rigidity of solid electrolytes enforces a 'one-in-one-out' mode of ion transport. In an electrolyte with a negative sublattice and a single mobile positive carrier, this phenomenon implies the absence of concentration gradients in the neutral bulk, as observed by Han et al. [7] and supported by the transference-number calculations of Siegel et al. [8]. Interfacial double layers in such materials screen most of the external electric field; the concomitant steep field gradients can lead to surface stresses that are much higher than the bulk, however [9]. Thus, a full picture of ion transport requires modelling the double layer and bulk together, to clarify the coupling among faradaic processes, diffusion, migration, charge screening, and mechanical deformation. Conventional Poisson–Nernst–Planck theory accounts for neither solute/solute interactions nor stress diffusion, motivating more sophisticated models to describe ion transport.

Goyal and Monroe [10] augmented the system of balance equations from Newman's concentrated-solution theory to account for solid elasticity, developing a dissipation function applicable to non-neutral, multi-species electrochemical systems. This result provides a basis for extending the Onsager–Stefan–Maxwell (OSM) equations for ion transport by applying the principles of irreversible thermodynamics [11]. Monroe and Delacourt [12] showed how OSM equations can be inverted to obtain transport laws in a modified Nernst–Planck form that illustrates how the ion mobilities in multi-species electrolytes are affected by ion/ion interactions. These preceding developments establish concentrated-solution theory as a powerful continuum framework for solid-electrolyte transport modeling.

This paper develops a transport model for solid ion conductors that contain multiple mobile charge carriers, using the garnet oxide electrolyte $Li_5La_3Nb_2O_{12}$ (LLNO) as a case study. Experiments have shown that this material is stable in proton-substituted forms with stoichiometries $Li_{5(1-y)}H_{5y}La_3Nb_2O_{12}$ [13], compositions we will abbreviate as $L_{1-y}H_yLNO$. We simulate $L_{1-y}H_yLNO$ slabs with global degrees of proton substitution spanning the range $0 \leq y \leq 1$, gathering literature data to determine all of the requisite phenomenological material properties.

* Corresponding author.
E-mail address: charles.monroe@eng.ox.ac.uk (C.W. Monroe).

https://doi.org/10.1016/j.electacta.2021.138563
0013-4686/© 2021 The Authors. Published by Elsevier Ltd. This is an open access article under the CC BY license (http://creativecommons.org/licenses/by/4.0/)

Presence of a secondary mobile carrier is found to enable lithium-concentration polarization, whose extent grows with applied current and is controlled by diffusional interactions between the two carriers. This in turn leads to voltage signatures characteristic of diffusion limitations, and causes materials with even a trace of proton substitution to exhibit a limiting current. At high currents the two carriers segregate, with the secondary carrier building up substantially near one of the electrode surfaces. Pressure build-up in interfacial double layers and volume-restricted ion diffusion in the bulk of the two-carrier material are studied, along with the transient dynamics of polarization. The limiting current density and Sand's transition time are computed for proton-substituted LLNO slabs, illustrating how the presence of a trace secondary carrier may influence solid-electrolyte performance and degradation.

1. Model formulation

General transport model. We assume an isothermal solid electrolyte composed of n chemically distinct species, indexed by subscript k. For each species, the molarity c_k and average species velocity $\vec{v}_k$ combine to yield the total molar flux $\vec{N}_k = c_k\vec{v}_k$. The electrolyte's mass density ρ is defined by introducing molar species masses M_k, such that $\rho = \sum M_k c_k$; the barycentric velocity $\vec{v}$ is defined through $\rho\vec{v} = \sum M_k\vec{N}_k$. Introduction of Faraday's constant F and equivalent species charges z_k allow one to define the excess charge density $\rho_e = F\sum z_k c_k$ and current density $\vec{i} = F\sum z_k\vec{N}_k$.

Locally, the excess charge density produces an external electric field $\vec{E}$, governed by Poisson's equation

$$\vec{\nabla}\cdot\left(\epsilon\vec{E}\right) = \rho_e, \tag{1}$$

where ϵ is the electrolyte's dielectric permittivity, taken to be constant. Species continuity is expressed by

$$\frac{\partial c_k}{\partial t} = -\vec{\nabla}\cdot\vec{N}_k \tag{2}$$

for $k = 1,\ldots,n$. A momentum balance relates system dynamics to the external mechanical stress $\vec{\vec{\sigma}}$ and electrostatic body forces $\rho_e\vec{E}$,

$$\rho\frac{\partial\vec{v}}{\partial t} + \rho\,\vec{v}\cdot\vec{\nabla}\vec{v} = -\vec{\nabla}\cdot\vec{\vec{\sigma}} + \rho_e\,\vec{E}\,. \tag{3}$$

Goyal and Monroe suggest that an additional diffusion stress can appear here because species in multicomponent materials convect momentum at their own velocities, rather than the mass-average velocity [10]. Diffusion stress is generally small and has been neglected.

Hirschfelder et al. applied principles of irreversible thermodynamics to show how flux laws in a multispecies system can be derived from an expression for local energy dissipation [11]. Given a statement of the dissipation function, one can identify conjugate pairs of species velocities and thermodynamic driving forces $\vec{d}_k$ that contribute to the energy losses associated with diffusion. OSM equations that describe how the driving forces balance the diffusional drag produced by the relative motion of species take the form

$$c_k\vec{d}_k = \sum_{j\neq k} K_{kj}\left(\vec{v}_k - \vec{v}_j\right), \tag{4}$$

in which K_{kj} is a coefficient that quantifies diffusional drag between species k and j. The dissipation function derived by Goyal and Monroe [10] shows that $\vec{d}_k$ breaks down into a mass-diffusion force, arising from the electrochemical potential gradient of species k, and a stress-diffusion force, from mechanical gradients. Expressing this force per mole of species k gives

$$\vec{d}_k = -\vec{\nabla}\mu_k + \frac{M_k}{\rho}\left(\vec{\nabla}p + \vec{\vec{\epsilon}}\,' : \vec{\nabla}\vec{\vec{\tau}}\right). \tag{5}$$

Here $\vec{\vec{\epsilon}}\,'$ is the deformation-strain tensor, p is the external pressure, and $\vec{\vec{\tau}} = \vec{\vec{\sigma}} - p\vec{\vec{I}}$ is the deformation stress. Because the Gibbs–Duhem relation requires that $\sum_k c_k\vec{d}_k = \vec{0}$, one only needs to write constitutive laws for $n-1$ driving forces in an n-ary diffusion system.

Composition variation, mechanical stress, and the electric field all contribute to the electrochemical-potential gradient of species k, through

$$\vec{\nabla}\mu_k = RT\sum_{j\neq m}\frac{\chi_{kj}}{\xi_k}\vec{\nabla}\xi_j + \overline{V}_k\left(\vec{\nabla}p + \vec{\vec{\epsilon}}\,' : \vec{\nabla}\vec{\vec{\tau}}\right) - Fz_k\vec{E}, \tag{6}$$

where sites in the crystal lattice are designated as species m. Here R is the gas constant and T is the absolute temperature; χ_{kj} is a thermodynamic factor, which describes how the logarithm of species k's activity varies with species j's lattice occupancy ξ_j, and $\overline{V}_k$ is the partial molar volume of species k.[1] The system of Eqs. 1 to 6 is closed by defining the lattice occupancy and stating constitutive laws for the thermodynamic material properties χ_{kj}, $\overline{V}_k$, and $\vec{\vec{\epsilon}}\,'$, as well as the transport properties K_{kj}.

Constitutive laws. We posit that the $L_{1-y}H_yLNO$ material can be treated as a ternary system ($n = 3$), in which lithium cations Li^+ are the primary charge carriers and protons H^+ are secondary carriers, and that both cations are able to occupy a single type of available site within the negatively charged oxide-crystal sublattice. Properties attributed to individual species are denoted by indices − (negatively charged lattice sites), + (lithium cations), and p (protons). Bearing in mind the Gibbs–Duhem constraint, we choose to write independent OSM laws for the forces $\vec{d}_+$ and $\vec{d}_p$.

A Stefan–Maxwell form, which introduces the diffusivity of species k through species j, $\mathscr{D}_{kj}$, is appropriate for the drag coefficients:

$$K_{kj} = \frac{RTc_kc_j}{c_-\mathscr{D}_{kj}}. \tag{7}$$

Onsager reciprocity guarantees that $K_{kj} = K_{jk}$, so $\mathscr{D}_{kj} = \mathscr{D}_{jk}$. Following the approach suggested by Fornasiero *et al.* [14], Eq. 7 has been modified from the form typically used for liquids, in that the lattice-site concentration c_-, rather than the total concentration of all species, appears in the denominator. This choice can alternatively be justified by a formal assumption that species moving in conductive channels have very small partial molar volumes compared to the lattice, $\overline{V}_+, \overline{V}_p << \overline{V}_-$, so that the total molar volume of the electrolyte depends very weakly on its lattice occupancy.

The Monroe–Delacourt process [12] converts Eqs. 4 and 5 into a modified form of Ohm's law,

$$\frac{\vec{i} - \rho_e\vec{v}_-}{\kappa} = \frac{\vec{d}_+}{Fz_+} + \left(1 - t_+^-\right)\left(\frac{\vec{d}_p - \zeta_{p+}\vec{d}_+}{Fz_p}\right), \tag{8}$$

and a flux-explicit transport law for $\vec{J}_p^- = c_p(\vec{v}_p - \vec{v}_-)$, the excess molar flux of protons relative to the lattice,

$$\vec{J}_p^- = \frac{\mathscr{D}_\times c_-}{RT}\left(\vec{d}_p - \zeta_{p+}\vec{d}_+\right) + \left(1 - t_+^-\right)\left(\frac{\vec{i} - \rho_e\vec{v}_-}{Fz_p}\right). \tag{9}$$

As well as the new parameter

$$\zeta_{p+} = \frac{z_p}{z_+}, \tag{10}$$

which expresses the ratio of the secondary carrier's charge to that of lithium, Eqs. 8 and 9 introduce three experimentally observable transport parameters: the ionic conductivity κ, the lithium

[1] Since extensivity of volume implies that $\sum c_k\overline{V}_k = 1$, the specification of partial molar volumes makes c_n a dependent variable, justifying the removal of the nth term from the sum in Eq. 6.

transference number relative to the lattice t_+^-, and the thermodynamic cross-diffusivity of mobile carriers, $\mathscr{D}_\times$. The set of macroscopic properties κ, t_+^-, and $\mathscr{D}_\times$ relates to the three microscopic Stefan–Maxwell diffusivities $\mathscr{D}_{+-}$, $\mathscr{D}_{\mathrm{p}+}$, and $\mathscr{D}_{\mathrm{p}-}$ *via* an invertible mapping dependent on the local concentrations of Li^+ and H^+.

It is natural to rescale carrier concentrations by introducing fractional lattice occupancies, defined as $\xi_+ = c_+/c_-$ and $\xi_\mathrm{p} = c_\mathrm{p}/c_-$ for Li^+ and H^+, respectively. We also introduce the symbol $\langle\xi_+^0\rangle = -z_-/z_+$ to represent the equilibrium lattice occupancy of carriers in the single-ion conductor limit (i.e., the equilibrium Li^+ occupancy of proton-free LLNO).

Some alternative parameter definitions help to express the macroscopic properties in more tangible terms. We first replace the lithium/lattice Stefan–Maxwell diffusivity $\mathscr{D}_{+-}$ with

$$\kappa_0 = \frac{F^2 z_+^2 c_- \langle\xi_+^0\rangle \mathscr{D}_{+-}}{RT}, \tag{11}$$

which represents the electrolyte's equilibrium ionic conductivity in the absence of the secondary carrier. That is, κ_0 is the electroneutral bulk conductivity of LLNO ($L_{1-0}H_0LNO$, in which $c_\mathrm{p} = 0$ uniformly). Two additional convenience parameters,

$$r_{\mathrm{p}-} = \frac{\mathscr{D}_{+-}}{\mathscr{D}_{\mathrm{p}-}} \quad \text{and} \quad r_{\mathrm{p}+} = \frac{\mathscr{D}_{+-}}{\mathscr{D}_{\mathrm{p}+}}, \tag{12}$$

express the diffusional resistances that protons place on the negative lattice and lithium ions, respectively, per unit of resistance the lattice exerts on lithium ions.

By manipulating the equations above, one can express all three macroscopic properties as functions of the local carrier occupancies:

$$\kappa = \frac{\kappa_0}{\langle\xi_+^0\rangle} \cdot \frac{r_{\mathrm{p}-}\xi_+ + \zeta_{\mathrm{p}+}^2\xi_\mathrm{p} + r_{\mathrm{p}+}(\xi_+ + \zeta_{\mathrm{p}+}\xi_\mathrm{p})^2}{r_{\mathrm{p}-} + r_{\mathrm{p}+}\xi_+ + r_{\mathrm{p}-}r_{\mathrm{p}+}\xi_\mathrm{p}}, \tag{13}$$

$$t_+^- = \frac{\xi_+[r_{\mathrm{p}-} + r_{\mathrm{p}+}(\xi_+ + \zeta_{\mathrm{p}+}\xi_\mathrm{p})]}{r_{\mathrm{p}-}\xi_+ + \zeta_{\mathrm{p}+}^2\xi_\mathrm{p} + r_{\mathrm{p}+}(\xi_+ + \zeta_{\mathrm{p}+}\xi_\mathrm{p})^2}, \tag{14}$$

and

$$\mathscr{D}_\times = \frac{RT\kappa_0}{F^2 z_+^2 c_- \langle\xi_+^0\rangle} \cdot \frac{\xi_+\xi_\mathrm{p}}{r_{\mathrm{p}+}(\xi_+ + \zeta_{\mathrm{p}+}\xi_\mathrm{p})^2 + r_{\mathrm{p}-}\xi_+ + \zeta_{\mathrm{p}+}^2\xi_\mathrm{p}}. \tag{15}$$

These functions of ξ_+ and ξ_p are parameterized by the properties κ_0, c_-, $\langle\xi_+^0\rangle$, $\zeta_{\mathrm{p}+}$, $r_{\mathrm{p}+}$, and $r_{\mathrm{p}-}$.

For simplicity we describe $L_{1-y}H_yLNO$ chemically as an ideal solid solution. In such a material the configurational entropy is the only composition-dependent part of the total entropy. A lattice-gas model can be used to establish the configurational contribution to the free energy, yielding a set of independent thermodynamic factors summarized as

$$\begin{bmatrix} \chi_{++} & \chi_{+\mathrm{p}} \\ \chi_{\mathrm{p}+} & \chi_{\mathrm{pp}} \end{bmatrix} = \begin{bmatrix} \frac{1-\xi_\mathrm{p}}{1-\xi_\mathrm{p}-\xi_+} & \frac{\xi_+}{1-\xi_\mathrm{p}-\xi_+} \\ \frac{\xi_\mathrm{p}}{1-\xi_\mathrm{p}-\xi_+} & \frac{1-\xi_+}{1-\xi_\mathrm{p}-\xi_+} \end{bmatrix}, \tag{16}$$

which has been defined so that it reduces to the identity matrix in the limit that $\xi_\mathrm{p} + \xi_+ << 1$.

Finally, we assume that all $L_{1-y}H_yLNO$ materials are isotropically linear-elastic [15], so that the mechanical state is determined by

$$\vec{\vec{\tau}} = \frac{3\,K(1-2\nu)}{(1+\nu)\overline{V}_-^\theta c_-}\vec{\vec{\epsilon}}', \tag{17}$$

in which K is the bulk modulus and ν is Poisson's ratio [16]. Thermodynamic consistency demands that shear modulus and volume have the same pressure dependence [10], so Eq. 17 is referenced to ambient pressure p^θ: the lattice's molar volume at ambient pressure, $\overline{V}_-^\theta$, normalizes c_- to extract its pressure dependence. Note also that, since the ideal-solid-solution assumption requires that configurational entropy accounts entirely for the composition dependence of free energy, $L_{1-y}H_yLNO$ must exhibit a composition-independent bulk modulus K. If K is constant with respect to external pressure p as well, then each partial molar volume necessarily varies with pressure as $\overline{V}_k(p) = \overline{V}_k^\theta \exp\left[-\left(p - p^\theta\right)/K\right]$.

Geometry and boundary conditions. Simulations will be performed to describe planar $L_{1-y}H_yLNO$ slabs of thickness L, sandwiched between two planar electrodes — spatially one-dimensional systems. As argued earlier [9,17], deformation stresses vanish in this configuration, and the normal stress in the x-direction relates simply to pressure, through $\sigma_{xx} = 3p - 2p^\theta$. One can also combine Eqs. 1 and 3, then integrate to produce an equation for local pressure in terms of E, the x-component of the electric field,

$$p(x) - p(0) = \frac{\epsilon}{6}\left[E^2(x) - E^2(0)\right]. \tag{18}$$

This result neglects inertial contributions to momentum, which are very small at practical current densities.

Both steady-state and transient simulations are performed under galvanostatic control at a constant current density i in the positive x-direction. In all cases it is assumed that the lattice is stationary, so that the x-component of its velocity, v_-, vanishes. We also assume that the electrodes participate in faradaic reactions that only involve Li^+ from the electrolyte. Thus the x-component of the excess proton flux J_p^- vanishes at both boundaries of the slab. It follows that the global proton content is conserved, such that

$$\frac{1}{L}\int_0^L \xi_\mathrm{p}(t,x)dx = \langle\xi_+^0\rangle y \tag{19}$$

at any time t. (In Eq. 19 the global extent of proton substitution y is used in exactly the same sense as in the compositional formula $L_{1-y}H_yLNO$.) Note that the boundary conditions $J_\mathrm{p}^- = v_- = 0$ at both boundaries also imply that the mass-average velocity in the x-direction within the electrolyte there is $v = iM_+/(\rho F z_+)$.

Following our earlier approach [9], we incorporate an interfacial characteristic frequency $(R_\mathrm{int}C_\mathrm{int})^{-1}$ as a model parameter to set the electric field at the boundaries: $E = R_\mathrm{int}C_\mathrm{int}i/\epsilon$. Values for lithium metal adjacent to garnet-type solid electrolytes yield time constants in the range $R_\mathrm{int}C_\mathrm{int} \sim 10^{-1\sim-3}$ s [18], implying that the interface is very capacitive and there is a much steeper polarization near interfaces than in the bulk. We use $2\pi R_\mathrm{int}C_\mathrm{int} = 10^{-1}$ s when considering reactive interfaces here.

When considering predictions of the transport model described above, the current density should be seen as a local, rather than a global, quantity. Differences between local and global currents can be induced by secondary non-uniformities. For example, sizing the solid electrolyte and electrodes differently can make the local current density differ from its average in different locations, affecting system performance [19–21].

Material properties. Most phenomenological properties of polycrystalline $L_{1-y}H_yLNO$ involved in this model can be found in the literature or are readily estimated. The molar masses of lithium and hydrogen are $M_+ = 6.941$ g mol^{-1} and $M_\mathrm{p} = 1.0079$ g mol^{-1}, respectively, and $M_- = 88.28$ g mol^{-1} is the mass of a carrier-free crystal formula unit (i.e., $La_3Nb_2O_{12}$) per mole of sites in its sublattice where carriers can reside (9 in this case, counting both 24c and 48g sites [22]). Both lithium cations and protons are monovalent, so $z_+ = z_\mathrm{p} = \zeta_{\mathrm{p}+} = 1$. Assuming pure LLNO is locally electroneutral at equilibrium, and that countercharges distribute uniformly across available lattice sites, $z_- = -5/9$. Consequently, the bulk lattice occupancy of LLNO is $\langle\xi_+^0\rangle = 5/9$.

The density of pure LLNO at 300 K and atmospheric pressure is $\rho^\theta = 5.170$ g cm^{-3} [23]. In line with the assertion that carrier concentration minimally affects lattice dimensions, we let $\overline{V}_+/\overline{V}_- =$

$\overline{V}_p/\overline{V}_- = 0.01$.[2] Hence the density measurement is consistent with a partial molar volume for sites of $\overline{V}_-^\theta = 17.728\ \mathrm{cm^3 mol^{-1}}$ and carrier partial molar volumes of $\overline{V}_+^\theta = \overline{V}_p^\theta = 0.177\ \mathrm{cm^3 mol^{-1}}$. LLNO has bulk modulus $K = 111.3$ GPa [25]. The equilibrium lithium concentration in proton-free LLNO is $c_+^{eq} = 31.2\ \mathrm{mol L^{-1}}$; impedance spectroscopy shows its relative permittivity to be 40 [26]. At 300 K the ionic conductivity of single-crystal LLNO is $\kappa_0 = 0.161\ \mathrm{mS cm^{-1}}$ [27], which can be used to estimate the lithium/lattice diffusivity $\mathscr{D}_{+-} = 1.397 \times 10^{-13}\ \mathrm{m^2 s^{-1}}$ through Eq. 11.

Experiments have shown that a range of $L_{1-y}H_yLNO$ materials with $0 < y < 0.82$ afford bulk conductivities nearly identical to pure LLNO [13]. In the bulk of an equilibrated electrolyte, local electroneutrality restricts composition such that $\xi_+ + \zeta_{p+}\xi_p = \langle\xi_+^0\rangle$. Thus, if the bulk conductivity is insensitive to y in $L_{1-y}H_yLNO$, then $\kappa/\kappa_0 = 1$ when $\xi_+ = \langle\xi_+^0\rangle - \zeta_{p+}\xi_p$, independent of ξ_p. Through Eq. 13, this requires that $r_{p-} = \zeta_{p+}$. Since $\zeta_{p+} = 1$ for $L_{1-y}H_yLNO$, the invariance of ionic conductivity with respect to y implies that Li^+ and H^+ have similar mobilities through the lattice: $\mathscr{D}_{p-} \approx \mathscr{D}_{+-}$. In short, the substitution invariance of macroscopic conductivity, which has been observed for materials including $L_{1-y}H_yLNO$ and $Li_{5(1-y)}H_{5y}La_3Sn_2O_{12}$ [28,29], implies that the lattice exerts similar drag forces on both carriers. Note that this conclusion about carrier mobilities relative to the lattice places no constraint on the drag that the Li^+ and H^+ species exert on each other.

The conditions $r_{p-} \approx \zeta_{p+}$ and $\zeta_{p+} = 1$ dramatically simplify the macroscopic properties, to the forms

$$\kappa = \frac{\kappa_0(\xi_p + \xi_+)}{\langle\xi_+^0\rangle}, \quad t_+^- = \frac{\xi_+}{\xi_p + \xi_+}, \quad \text{and}$$
$$\mathcal{D}_\times = \frac{RT\kappa_0\xi_p\xi_+}{F^2 z_+^2 c_- \langle\xi_+^0\rangle(\xi_p + \xi_+)[1 + r_{p+}(\xi_p + \xi_+)]}. \tag{20}$$

Thus the conductivity of $L_{1-y}H_yLNO$ is proportional to total lattice occupancy, and its lithium transference number is just the fraction of occupied sites containing lithium. Cross-diffusivity is the only transport property affected by carrier/carrier drag interactions.

Although literature values are unavailable for r_{p+}, thermodynamic considerations help to constrain its range. The second law of thermodynamics requires that the instantaneous dissipation of energy associated with Eq. 4 must be positive. Given that $\kappa_0 > 0$ and $r_{p-} \approx 1$, it follows from an analysis of the bulk material near equilibrium that

$$r_{p+} > -\frac{1}{\langle\xi_+^0\rangle}. \tag{21}$$

Interestingly, negative values of this parameter are possible, suggesting that flow of protons can facilitate lithium diffusion in some circumstances, rather than slowing it.

A primary objective of this work is to explore how carrier/carrier interactions, described by the parameter r_{p+}, affect the electrolyte's electrochemical response. To facilitate the presentation of results across the entire range of possible carrier/carrier interactions, we introduce an interaction strength parameter ψ, related to r_{p+} through

$$r_{p+} = \frac{1}{\langle\xi_+^0\rangle}\left(\frac{1+\psi}{1-\psi} - 1\right). \tag{22}$$

This establishes an order-preserving, invertible map between the closed domain $\psi \in [-1, 1]$ and the semi-infinite domain $r_{p+} \in [-1/\langle\xi_+^0\rangle, \infty)$ that maps $r_{p+} = 0$ to $\psi = 0$. If the carrier/carrier interaction strength is zero, then the two carrier ions move independently; diffusional drag on them is controlled only by their interactions with the crystal lattice, as is assumed when electrolytes are described by Poisson–Nernst–Planck theory. If the interaction strength is positive, opposing motion of the two carriers increases diffusional drag, in line with natural expectations for concentrated diffusion systems. For example, the motion of protons can augment drag on lithium above what it already feels from the lattice, similar to how defects slow lithium transport in $LiFePO_4$ [30]. When the carrier/carrier interaction strength is negative, opposing motion of the carriers reduces diffusional drag. This can occur via collective transport modes such as the formation of ion pairs, as has been suggested to explain ionomers that exhibit negative transference numbers [31].

2. Double-layer effects

The impact of global proton substitution y was first studied assuming no diffusional drag between mobile carriers, $r_{p+} = 0$ (interaction strength $\psi = 0$), consistent with the elementary assumptions of Nernst–Planck transport theory. Fig. 1 shows simulated steady-state property distributions at $i = 0.1\ \mathrm{mA cm^{-2}}$ in pure LLNO, $y = 0$, and in $L_{1-y}H_yLNO$ at $y = 0.25$, 0.5, and 0.75. In proton-free LLNO, lithium ions distribute uniformly in the bulk, consistent with the observations by Han et al. [7]. Space-charge layers build up near the interfaces to screen the external electric field, as can be seen in Fig. 1c. This space charging causes pressure to build up near the interfaces, shown in Fig. 1d. This pressure buildup in double layers arises from Lorentz body forces, which lead to stress in accord with Eq. 18.

The presence of multiple cations affects ion distributions differently in the bulk electrolyte than in the interfacial double layers. Since the double layers screen the field due to surface charging, the bulk is relatively electroneutral locally. The bulk Li^+ concentration falls in the direction of the current and, because the negative crystal lattice is immobile, the H^+ concentration rises to maintain neutrality. This bulk-concentration polarization varies with the global extent of lithium substitution, becoming larger for both carriers as y increases. Near the electrolyte's edges, where local electroneutrality is violated, the sign of the lithium-occupancy gradient opposes its sign in the bulk. The double-layer responses are relatively similar at different global proton contents; because both carriers have the same equivalent charge ($\zeta_{p+} = 1$), the ionic strength of $L_{1-y}H_yLNO$ — and consequently, its Debye screening length — does not depend on y.

Fig. 2 illustrates steady-state carrier distributions in $L_{0.5}H_{0.5}LNO$, showing the responses of materials identical save for the strength of the Li^+/H^+ diffusional interaction. Three types of carrier/carrier interactions are possible, corresponding to positive, zero, and negative interaction strength ψ: Fig. 2 compares cases with $r_{p+} = -1$ and 1 ($\psi = -5/13$ and $5/23$, respectively) to the non-interacting case from Fig. 1. Carrier/carrier interactions affect bulk polarization substantially. When interaction strength is positive, the presence of H^+ slows Li^+ transport, increasing bulk polarization relative to the non-interacting case; when it is negative, the opposite is observed.

As the space-charge layer adjacent to the negative electrode screens the electric field, it accumulates a higher total carrier content than the relatively electroneutral region immediately outside it; the total carrier content near the positive electrode is lower. For extremely thin systems, the minimum lithium content therefore occurs at the anode, leading to a limiting current controlled by space charging. When the electrolyte is much thicker than the Debye length, however, bulk carrier profiles achieve a qualitative appearance like Figs. 1 and 2: the lithium occupancy reaches its min-

[2] In electrolytes such as $L_{1-y}H_yLNO$, the partial molar volumes of both Li^+ and H^+ are extremely small relative to that of the negative sublattice. Ion-size effects depend on the absolute difference between the carriers' partial molar volumes and are therefore neglible here. When this difference is large, there can be considerable ion-size effects in the double layer, as has been shown for ionic-liquid-based lithium electrolytes [24].

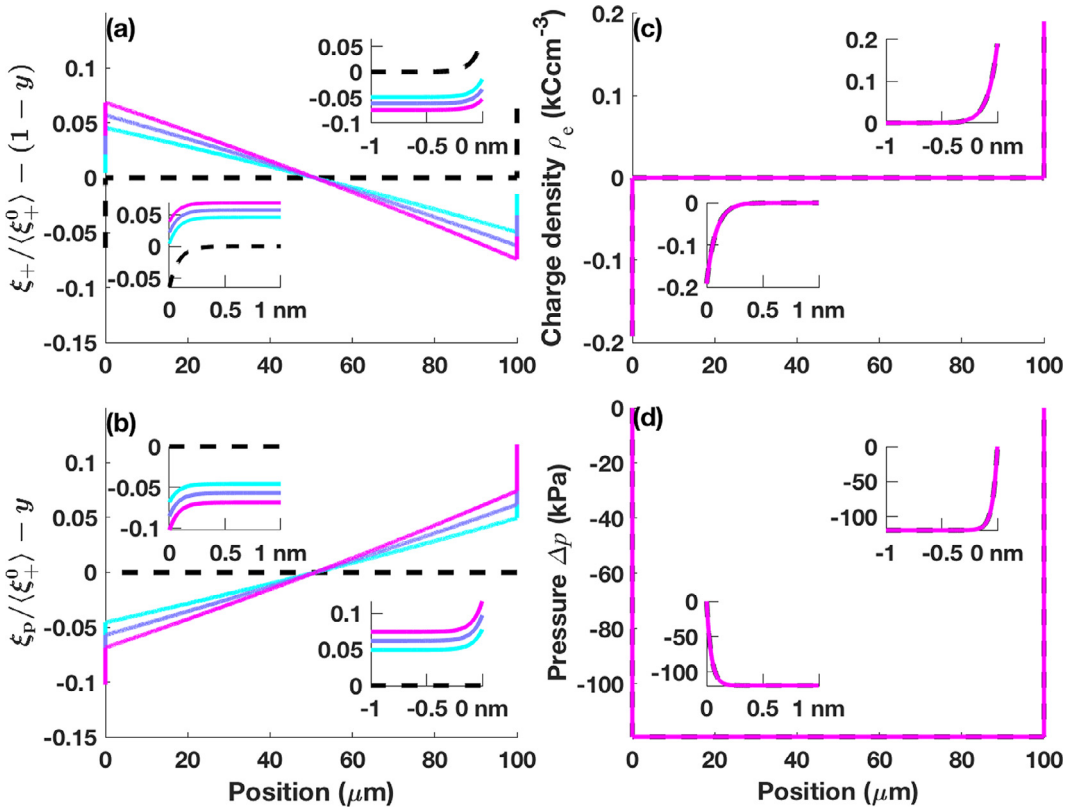

Fig. 1. Profiles of steady-state (a) lithium content, (b) proton content, (c) charge density, and (d) relative pressure $\Delta p = p(x) - p(0)$ for planar solid-electrolyte slabs between electrodes reversible to lithium cations, under an applied current density $i = 0.1$ mAcm^{-2}. Black dashed lines represent proton-free LLNO ($Li_5La_3Nb_2O_{12}$). The colored lines correspond to $L_{1-y}H_yLNO$ ($Li_{5(1-y)}H_{5y}La_3Nb_2O_{12}$) samples with no carrier/carrier interaction strength, $\psi = r_{p+} = 0$, but with different global extents of proton substitution: $y = 0.25$ (cyan), 0.5 (purple), and 0.75 (magenta). Inset plots focus on the double layers near the electrolyte's edges, with horizontal axes indicating position relative to the nearest boundary. (For interpretation of the references to colour in this figure legend, the reader is referred to the web version of this article.)

imum in the transition zone between the cathodic space-charge layer and the bulk — about 10 Debye lengths from the negative-electrode surface. The minimum lithium occupancy and the limiting current are entirely determined by bulk lithium transport when electrolyte slabs are far greater than 20 Debye lengths thick. Since all synthetic techniques we are aware of produce electrolyte slabs more than one micrometer thick, which is far greater than 20 Debye lengths, we focus on that regime for the remainder of this study.

3. Steady-state polarization

To elucidate the diffusion-controlled responses of electrolyte slabs more than a micrometer thick, the general model was simplified by assuming local charge neutrality. Since electroneutrality implies that Lorentz forces vanish and inertia remains of higher order, Eq. 3 shows that the pressure becomes uniform: $\vec{\nabla} p \approx 0$. Eq. 9 becomes

$$\vec{J_p}\big|_{\rho_e=0} = -\mathscr{D}_\times \chi c_- \vec{\nabla} \ln \xi_p + \frac{\left(1 - t_+^-\right)\vec{i}}{F z_p}. \tag{23}$$

The electroneutral Darken factor χ introduced here depends on local composition through

$$\chi = \frac{\langle\xi_+^0\rangle\left(1 - \langle\xi_+^0\rangle\right) - \zeta_{p+}(1 - \zeta_{p+})\xi_p}{\left[1 - \langle\xi_+^0\rangle - (1 - \zeta_{p+})\xi_p\right]\left(\langle\xi_+^0\rangle - \zeta_{p+}\xi_p\right)}, \tag{24}$$

a form identified by inserting Eqs. 5, 6, and 16 into the diffusion driving force that appears in Eq. 9, then using the electroneutrality constraint to eliminate ξ_+. When $\zeta_{p+} = 1$, as it does for $L_{1-y}H_yLNO$, this can be used to show that Eq. 23 becomes

$$\vec{J_p}\big|_{\rho_e=0} = -\frac{RT\kappa_0(1-\psi)}{F^2 z_+^2 \langle\xi_+^0\rangle(1+\psi)}\vec{\nabla}\xi_p + \frac{\xi_p \vec{i}}{F z_p \langle\xi_+^0\rangle} \tag{25}$$

after insertion of Eqs. 13 through 15 and 22.

Under local electroneutrality the current density is always constant with respect to x, and at steady state the proton flux vanishes uniformly. Thus, Eq. 25 produces a simple differential equation in ξ_p,

$$\frac{d \ln \xi_p}{d(x/L)} = \frac{F z_+ L(1+\psi)}{RT\kappa_0(1-\psi)} \cdot i = I, \tag{26}$$

wherein the rightmost equality introduces a dimensionless current density, I. Direct integration and use of Eq. 19 to specify the unknown constant yields

$$\xi_p(x) = \frac{I\langle\xi_+^0\rangle y}{\exp\left[I\left(1 - \frac{x}{L}\right)\right] - \exp\left(-I\frac{x}{L}\right)}, \tag{27}$$

the steady-state proton distribution. This result also determines the lithium distribution because local electroneutrality requires that $\xi_+(x) = \langle\xi_+^0\rangle - \xi_p(x)$.

Eq. 27 rationalizes the relatively linear shapes of the carrier distributions seen outside the double layers in Figs. 1 and 2. When $I << 1$, Eq. 27 shows that

$$\frac{\xi_p}{\langle\xi_+^0\rangle y} = 1 + \left(\frac{x}{L} - \frac{1}{2}\right)I + \mathcal{O}\left(I^2\right). \tag{28}$$

In the case of a 100 μm thick sample driven at 0.1 mAcm^{-2}, the dimensionless current is $I = 0.24$ with the material properties

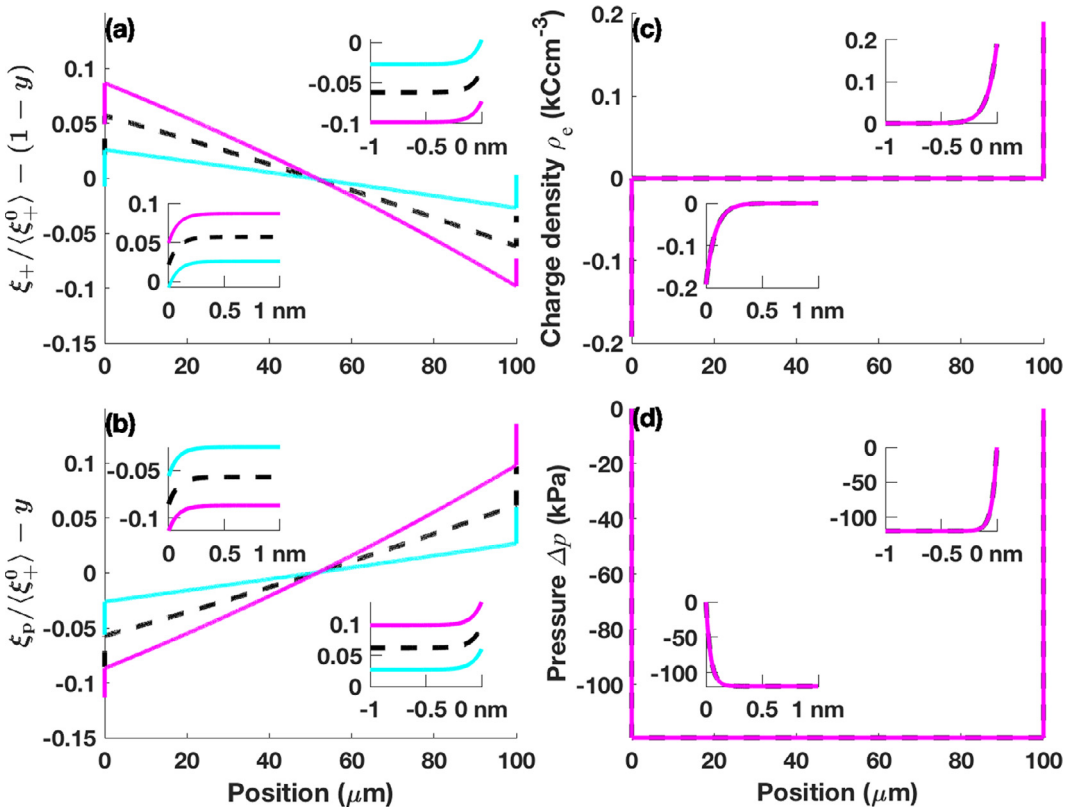

Fig. 2. Profiles of steady-state (a) lithium content, (b) proton content, (c) charge density and (d) relative pressure $\Delta p = p(x) - p(0)$ in planar $L_{0.5}H_{0.5}LNO$ slabs between electrodes reversible to lithium cations, under an applied current density of $i = 0.1$ mAcm^{-2}. The black dashed lines show the $L_{0.5}H_{0.5}LNO$, $r_{p+} = \psi = 0$ case from Fig. 1 for reference. Colored lines correspond to samples with (cyan) negative interaction strength $\psi = -5/13$ ($r_{p+} = -1$); and (magenta) positive interaction strength, $\psi = 5/23$ ($r_{p+} = 1$). Inset plots focus on the double layers near the electrolyte's edges, with horizontal axes indicating position relative to the nearest boundary.

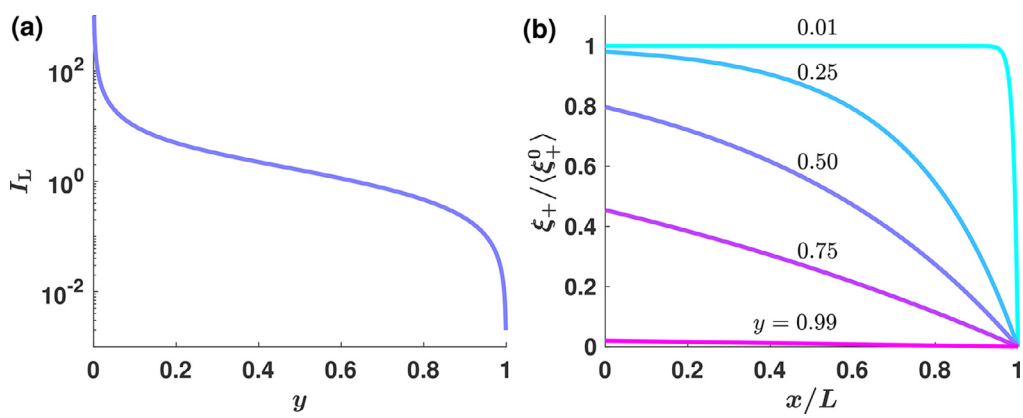

Fig. 3. (a) Dimensionless limiting current density I_L for $L_{1-y}H_yLNO$; (b) Steady-state lithium distribution at the limiting current density for $L_{1-y}H_yLNO$ slabs between electrodes reversible to lithium.

given above when $\psi = 0$. Higher-order corrections to the linear distribution are therefore relatively small for the case studied in the prior section. Note that, as well as predicting the shape of the proton distributions in Figs. 1 and 2, Eq. 28 also accurately predicts the difference in proton content across the neutral bulk.

For materials with $0 < y < 1$, current may cause the lithium occupancy to vanish at a boundary, corresponding to a traditional limiting current density. Let $\xi_p(L) = \langle \xi_+^0 \rangle$ when I reaches this dimensionless limiting current density, I_L. Eq. 27 gives

$$y = \frac{1 - \exp(-I_L)}{I_L}, \tag{29}$$

a formula relating the dimensionless parameter I_L to the global proton content. Fig. 3 shows how the dimensionless limiting current and the steady-state lithium distribution at the limiting current vary with respect to y in $L_{1-y}H_yLNO$. Observe that both can be computed without considering the carrier/carrier interaction strength.

Unsurprisingly, the limiting current increases monotonically as the extent of lithium substitution by protons falls. The shapes of the steady-state lithium distributions change significantly, however. When the extent of lithium substitution is large, $y > 0.75$, the lithium distribution is relatively linear, even at the limiting current. As the extent of substitution becomes lower, the lithium distribution at the limiting current is increasingly nonlinear, showing concavity in the range $0.25 < y < 0.5$. At smaller extents of lithium substitution, $y < 0.25$, the lithium distributions obtain qualitatively

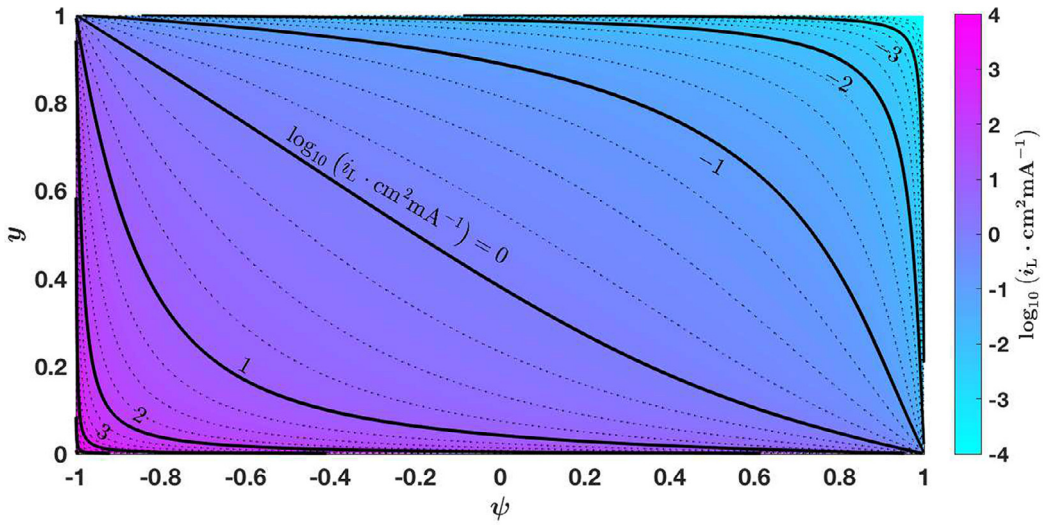

Fig. 4. Dimensional limiting current density i_L for a 100 μm $L_{1-y}H_yLNO$ slab, presented as a contour plot with respect to the global extent of lithium substitution y and the carrier/carrier interaction strength ψ.

different shapes — a diffusion boundary layer appears near the cathode.

Analysis of Eqs. 27 and 29 shows that when $I_L >> 1$, the thickness of the cathodic diffusion boundary layer scales as L/I_L. Thus trace substitution of lithium by protons may encourage carrier segregation, causing substantial proton accumulation near the cathode. This effect is consistent with experimental observations, which have shown that dopants accumulate at interfaces with solid lithium-ion conductors and grain boundaries within them [32]. As well as impacting local transport properties significantly [33], changes in the carrier balance near interfaces can facilitate electrolyte degradation [34].

Expressed in dimensional terms, the limiting current density i_L is

$$i_L = \frac{RT\kappa_0}{Fz_+L} \cdot \left(\frac{1-\psi}{1+\psi}\right) \cdot I_L(y), \tag{30}$$

wherein the dimensionless function $I_L(y)$ is determined implicitly by Eq. 29. To provide a sense of scale: i_L would be 0.67 mA cm^{-2} for a 100 μm slab of single-crystal $L_{0.5}H_{0.5}LNO$ material in which $\psi = 0$. Notably, this is of the same order as the critical currents that have been observed for other oxide garnet lithium conductors [18,35,36]. If a solid electrolyte admits multiple charge carriers, diffusion limitations may make its interfaces susceptible to morphological instability during lithium deposition. Observe also that boundaries and defects within polycrystalline LLNO can reduce the conductivity by two or more orders of magnitude from the single-crystal conductivity [13]. When the overall conductivity of a polycrystalline sample is lower, Eq. 30 shows that the limiting current density will be smaller by the same proportion, making diffusion limitations even more of a concern.

Fig. 4 uses Eq. 30 to present quantitatively how both proton content y and Li^+/H^+ interaction strength ψ affect the limiting current density of 100 μm thick $L_{1-y}H_yLNO$ slabs with lithium-reversible interfaces. Although higher proton content generally lowers the limiting current, consistent with the plot in Fig. 3a, the scale of the limiting current is greatly affected by carrier/carrier interaction strength. At a given global proton content, negative interaction strength can increase the limiting current by orders of magnitude. Even with weak interaction strength, diffusion limitations are not of great concern if the degree of lithium substitution is low: when $y < 0.3$ and $\psi \approx 0$, i_L is always more than 1 mA cm^{-2}.

The well studied $Li_7La_3Zr_2O_{12}$ (LLZO) electrolyte has a conductivity of 0.4 mS cm^{-1} [18,37] — about twice that of single-crystal LLNO — but resists lithium substitution by other mobile carriers [38]. Trends seen from Fig. 4 suggest that the diffusion-limited current density of an LLZO slab should far exceed 10 mA cm^{-2}; this is well over an order of magnitude larger than the experimentally observed critical current at which dendrites initiate in that material [18]. Broadly speaking, critical currents in thin, high-conductivity, defect-free solid electrolytes ($L/\kappa < 100$ Ωcm^2) likely do not owe to the presence of secondary carriers. If a sample has lower bulk conductivity, contains more impurities or defects, or has higher resistance because it is thicker, the limiting current density can fall by orders of magnitude, in accord with Eqs. 29 and 30. In such situations, lithium depletion at the cathode needs to be considered as a potential driver of electrolyte failure.

4. Galvanostatic transients

Since lithium depletion at the cathode can facilitate degradation, it is worthwhile to investigate the timescale with which steady-state concentration profiles develop. After inserting the locally electroneutral proton flux from Eq. 25 into the proton balance from Eq. 2, one arrives at the convective diffusion equation

$$\frac{\partial \xi_p}{\partial \tau} + IL\frac{\partial \xi_p}{\partial x} = L^2\frac{\partial \xi_p}{\partial x^2}, \tag{31}$$

in which the dimensionless time τ is defined as

$$\tau = \frac{RT\kappa_0(1-\psi)t}{F^2 z_+^2 \langle \xi_+^0 \rangle c_-(1+\psi)L^2}. \tag{32}$$

A spatial first derivative appears in Eq. 31 due to the composition dependence of lithium transference. Thus the dimensionless current I is revealed to be formally analogous to a Péclet number, although its appearance in the proton balance owes to migration (carrier drift), rather than convection.

Eq. 31 was solved to simulate the response at times $\tau > 0$ to a step change up to dimensionless current I, for a $L_{1-y}H_yLNO$ slab in an initially equilibrated state such that $\xi_p(0,x) = y\langle \xi_+^0 \rangle$. Again it was assumed that the electrodes were selective to lithium exchange, implying instantaneous transient no-flux boundary conditions for protons, $J_p|_{\tau,0} = J_p|_{\tau,L} = 0$.

In their work on faradaic convection in liquid electrolytes, Liu and Monroe [39] provided a Fourier-series solution to an exactly

analogous convective-diffusion system. Beyond the usual problem that Fourier series require large numbers of terms for accuracy at short times, they found that the series exhibits the Gibbs phenomenon. An alternative solution methodology was therefore developed, to produce closed-form analytical results that work well at short times and also predict the proton content precisely at particular locations.

Relaxation to the steady state Laplace transformation with respect to time changes the partial differential system to an ordinary system with constant coefficients and linear Robin boundary conditions, whose solution is parameterized by the Laplace variable s_L, as well as I. An exact solution for the transformed proton-fraction distribution was obtained, and was then rearranged into a product of two transforms, one of which was a rational function of $u = \exp(-k\sqrt{s_L})$ with $k > 0$; this rational function was Taylor expanded around $u = 0$ to produce an equivalent expression of the transform as an infinite sum, amenable to inversion term-by-term.[3] This yields a pointwise convergent form for the transient proton distribution that does not exhibit the Gibbs phenomenon, given analytically by

$$\frac{\xi_p\left(\tau, \frac{x}{L}, I\right)}{\langle \xi_+^0 \rangle y} = 1 + I \sum_{k=0}^{\infty} e^{\frac{I}{2}} g_{2k+1}\left(\tau, \frac{x-L}{L}, I\right) - \sum_{k=0}^{\infty} e^{-\frac{I}{2}} g_{2k+1}\left(\tau, \frac{x}{L}, I\right), \tag{33}$$

in which the basis functions g_k are

$$g_k(\tau, \alpha, I) = e^{\frac{I\alpha}{2}} [f_k(\tau, \alpha, I) + f_k(\tau, -\alpha, -I)], \tag{34}$$

and the subsidiary function f_k, defined as

$$f_k(\tau, \alpha, I) = \frac{1}{2I} e^{\frac{1}{2}(k+\alpha)I} \mathrm{erfc}\left(\frac{k+\alpha+I\tau}{2\sqrt{\tau}}\right) - \frac{1}{2I} e^{-\frac{1}{2}(k+\alpha)I} \mathrm{erfc}\left(\frac{k+\alpha-I\tau}{2\sqrt{\tau}}\right) - \sqrt{\tau} e^{\frac{1}{2}(k+\alpha)I} \mathrm{ierfc}\left(\frac{k+\alpha+I\tau}{2\sqrt{\tau}}\right), \tag{35}$$

is phrased in terms of the error function complement and its first integral.[4] With sums truncated after the fifth terms, Eq. 33 produces results that differ by less than 5×10^{-11} everywhere from the steady-state profile at $\tau = 1$. Since the series expansion technique suggests that fewer terms should be needed at shorter times, this number of terms probably suffices in most situations. The close agreement further suggests that the condition $\tau = 1$ is a very conservative estimate of the time needed to reach the steady state.

The transient relaxation of the $L_{0.5}H_{0.5}LNO$ system in response to a step change up to the limiting current density is presented in Fig. 5. Just after the current step ($\tau = 0.001$), concentration gradients appear at the electrolyte's boundaries as lithium is produced or consumed there. Note that there is a small difference between the slopes at either end of the electrolyte, with the slope at the negative boundary, $x = L$, generally steeper than that at the positive boundary, $x = 0$. This difference owes to the composition-dependent transference number, which produces the convection-like term in Eq. 31. The disparity between slopes becomes greater as the proton occupancy approaches its steady state because the lithium transference number at the positive boundary becomes larger than at the negative.

The transient and steady-state distributions in Fig. 5 agree within 0.001 at $\tau = 0.32$, about half the value expected for the classical galvanostatic electrolyte-diffusion problem with constant transference. Given the baseline properties of $L_{0.5}H_{0.5}LNO$ reported above, this suggests that the steady distributions shown in Figs. 1 and 2 are reasonable depictions of the system's state after current has been applied for a period of the order of 1–10 hours — a range whose upper end is far longer than a typical battery cycle. It is significant that practical cycling experiments in materials like $L_{0.5}H_{0.5}LNO$ likely induce a purely transient mode of response, rather than a pseudo-steady one. Also, samples should be expected to take several hours to relax to equilibrium after being subjected to applied current.

Two significant factors control the shape of the transient proton distribution. At short times there is a diffusion boundary layer whose thickness grows with $\sqrt{\tau}$, so the proton distribution varies with $1/\sqrt{\tau}$, as in typical film-penetration diffusion. Penetration depth in the present problem is also affected by migration, however, as determined by the net charge exchanged, which scales dimensionlessly as $I\tau$. The analytical solution provided by Eqs. 33 through 35 can be viewed as a sum over a train of characteristic, evanescent wavelike solutions that propagate at velocity I in the direction of increasing or decreasing x, which emanate from the inner and outer edges of the electrolyte. Since this effect penetrates only as far as the edges of the concentration boundary layers, the effective linear charge density input into them, $I\sqrt{\tau}$, arises as a second parameter that also controls system relaxation. Ultimately, when analyzing asymptotic behavior of this problem at a given instant, one also needs to consider how the value of parameter β, defined as

$$\beta = \frac{I\sqrt{\tau}}{2}, \tag{36}$$

compares to the inverse diffusive penetration depth $1/(2\sqrt{\tau})$.

Sand's time When the current density applied to the electrolyte is above the limiting current, $I = sI_L$, with $s > 1$, there will be a finite transition time, commonly known as Sand's time, at which the lithium occupancy vanishes at one electrolyte boundary and the voltage needed to maintain the current will suddenly rise. The implicit formula

$$\xi_p(\tau_{Sand}, 1, sI_L(y)) = \langle \xi_+^0 \rangle y, \tag{37}$$

derived from Eq. 33, yields Sand's time τ_{Sand} in terms of the global proton fraction y and the current multiplier s. This function is presented as a contour plot of β_{Sand} in Fig. 6a.

The figure shows that β_{Sand} varies over about three orders of magnitude depending on the global proton content. Generally, smaller proton contents produce larger values of β_{Sand}. When the current multiplier has moderate values, in the range $1 < s < 2$, the coupling between diffusion and migration is significant and higher-order terms in Eq. 33 are important. When the current multiplier is high, $s > 2$, β_{Sand} reaches a constant value dependent only on y. In this case, the higher-order terms in Eq. 37 become negligible and

$$\left(2\beta_{Sand}^2 + 1\right)\mathrm{erfc}(\beta_{Sand}) - \frac{2\beta_{Sand}}{\sqrt{\pi}} e^{-\beta_{Sand}^2} \approx \frac{1}{y}. \tag{38}$$

This high-current expression can be used to interpret the results of galvanostatic polarization experiments run far above the limiting

[3] The Fourier series of Liu and Monroe [39] can be obtained from the same Laplace transform by an alternative approach based on a Mittag-Leffler pole expansion, as follows: express the exact transformed proton distribution as a single fraction; examine the roots of the denominator to produce a formula for the location of the nth pole, bearing in mind that causality of the Laplace transform mandates that all the poles lie in one half of the complex plane; then apply Cauchy's residue theorem to cast the Bromwich integral as a sum over all n.

[4] Abramowitz and Stegun [40] define

$$\mathrm{ierfc}(z) = \int_z^{\infty} \mathrm{erfc}(z)dz = \frac{1}{\sqrt{\pi}} e^{-z^2} - z\,\mathrm{erfc}(z).$$

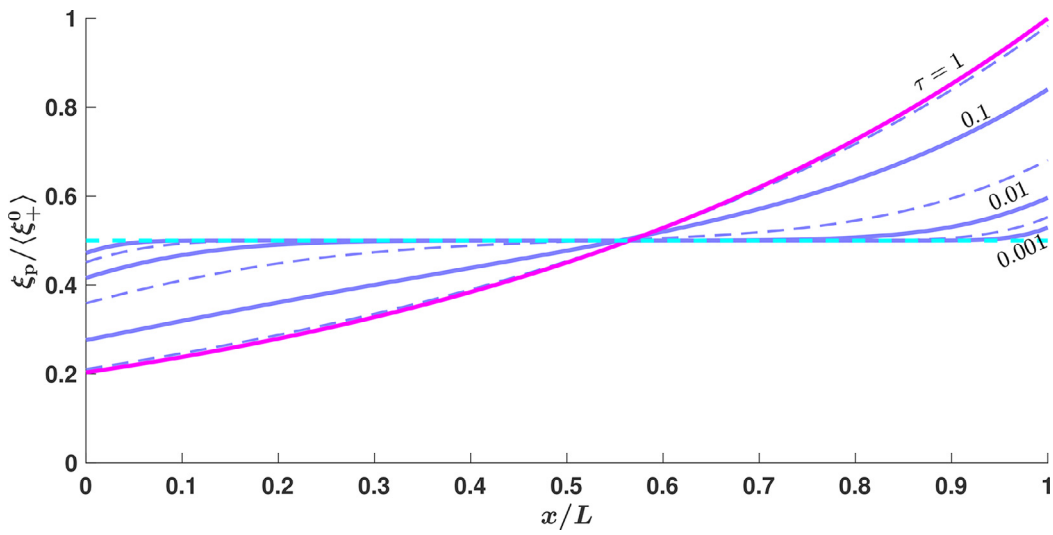

Fig. 5. Transient proton-occupancy distributions ξ_p in a $L_{0.5}H_{0.5}LNO$ slab subjected to a from open circuit up to the limiting current. A dashed cyan line shows the open-circuit equilibrium state at $\tau = 0$. Solid purple lines show dimensionless times $\log_{10}\tau = -3$, -2, and -1, and dashed purple lines indicate half-integer values of $\log_{10}\tau$. A solid magenta line shows the steady-state distribution from Eq. 27, which differs from Eq. 33 by less than 0.001 everywhere at $\tau = 0.32$. (For interpretation of the references to colour in this figure legend, the reader is referred to the web version of this article.)

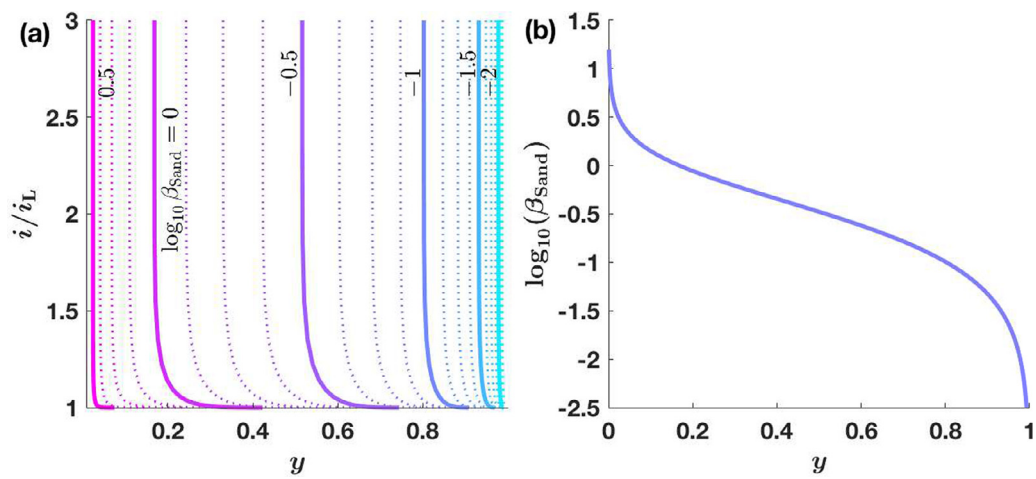

Fig. 6. (a) Parameter $\beta_{Sand} = \frac{1}{2}I\sqrt{\tau_{Sand}}$ as a function of limiting-current multiplier s and the extent of lithium substitution by protons, y. When the multiplier is sufficiently high ($s > 2$), β_{Sand} becomes independent of current and its contours become vertical. (b) Parameter β_{sand} as a function of proton fraction y in the $s > 2$ limit.

current. Solutions of this implicit equation are presented graphically on Fig. 6b. Unlike what one would expect from typical diffusion systems, β_{Sand} is not a universal constant; its variation with y owes to the composition dependence of lithium transference.

Since the dynamics of the proton distribution is determined by lithium/proton interactions, experimental measurements of Sand's time may be a useful route to establish the interaction strength ψ. Combining Eqs. 32, 36, and 37 yields a dimensional formula for Sand's time at a given current density i ($> 2i_L$) as a function of global proton content y as well as ψ,

$$t_{Sand}(i, y, \psi) = 4\kappa_0 c_-\langle\xi_+^0\rangle RT\left(\frac{1+\psi}{1-\psi}\right)\cdot\left(\frac{\beta_{Sand}}{i}\right)^2. \tag{39}$$

Usefully, the sample thickness does not appear here, although it is involved in the choice of applied current, because it determines i_L through Eq. 30. This result shows that the combined parameter $t_{Sand}i^2$ depends only on material properties when $i > 2i_L$.

Variations in microstructure and grain-boundary conditions generally reduce the apparent conductivity of $L_{1-y}H_yLNO$. Fig. 7 shows ψ as a function of the extent of lithium substitution y and the experimentally measurable combined parameter $t_{Sand}i^2$. Two cases are studied: one with the single-crystal $L_{0.5}H_{0.5}LNO$ properties given above, and a second with properties of the polycrystalline material, for which κ_0 was assumed to be 100 times smaller than the single-crystal value [27], commensurate with the room-temperature data of Truong et al. [13]. A more negative carrier/carrier interaction strength generally yields a shorter Sand's time. In both examples, at a given proton content and applied current, Sand's time varies by an order of magnitude in the window where ψ varies from -0.5 to 0.5. The drop in conductivity associated with polycrystallinity dramatically affects how ψ, y, and $t_{Sand}i^2$ relate.

A comparison between Fig. 7a and b indicates that smaller conductivity gives a smaller Sand's time in general. When a current density of 10 mA cm^{-2} is applied to $L_{0.5}H_{0.5}LNO$ with $-0.5 < \psi < 0.5$, Sand's time ranges from 30 s to 5 min for single-crystal samples, and from 3 s to 30 s for less conductive polycrystalline samples. Observe that making the conductivity higher — say, by increasing the ambient temperature — would be expected to have the opposite effect, lengthening Sand's time by raising the limiting current.

Dendrite formation as a result of lithium depletion near the cathode could be a problem for less conductive, multicarrier solid electrolytes operated at current densities in the range of 0.1 –

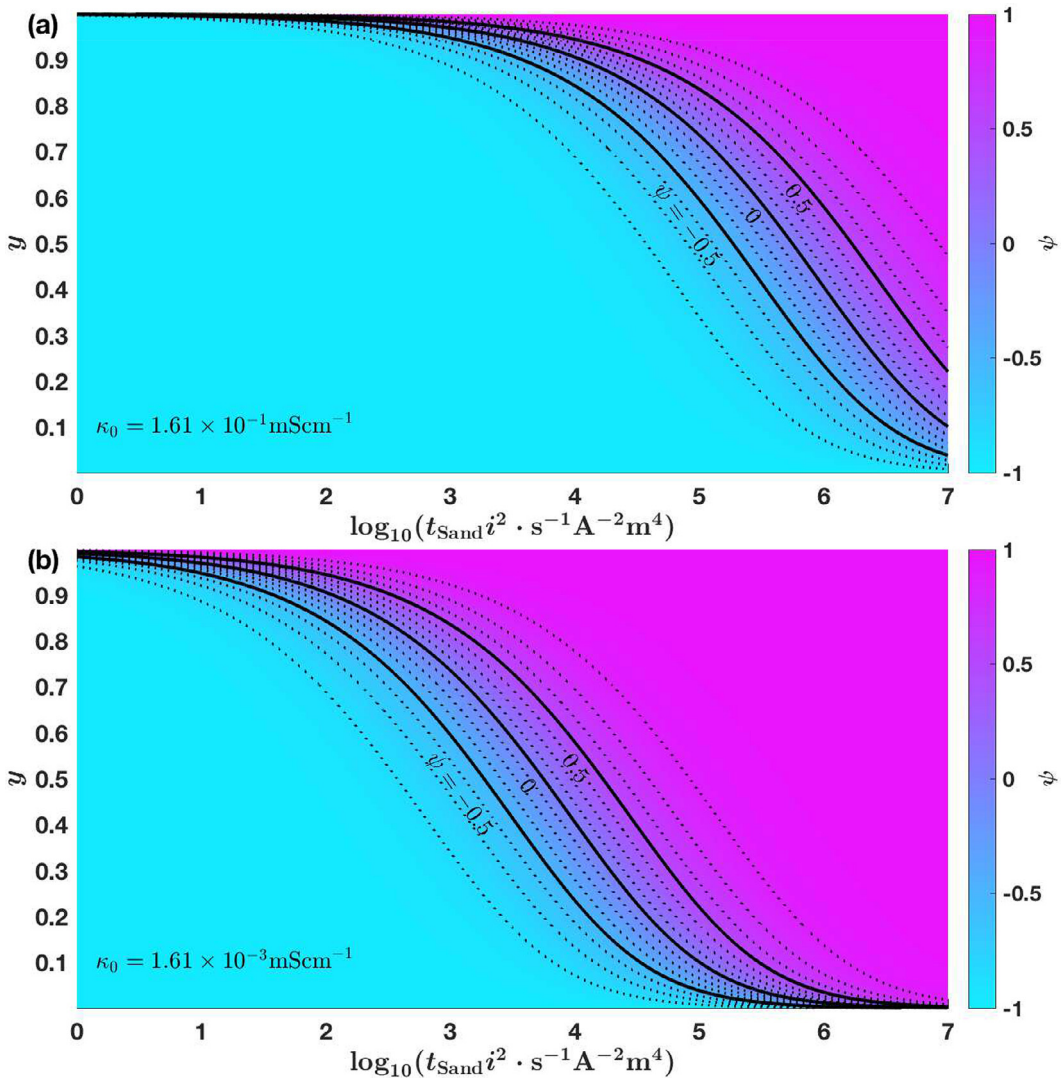

Fig. 7. Dependence of lithium/proton interaction strength ψ on the Sand's time t_{Sand}, applied current density i, and the global extent of lithium substitution y when the limiting-current multiplier is greater than 2. (a): Data for single-crystal $L_{0.5}H_{0.5}LNO$, for which $\kappa_0 = 0.161$ mScm^{-1} [27]; (b) Data for polycrystalline $L_{0.5}H_{0.5}LNO$, with κ_0 two orders of magnitude smaller [13].

10 mAcm^{-2}. Notably, this is commensurate with the magnitudes of critical current densities that have been observed for some solid-oxide electrolytes [18,35,36,41].

5. Conclusions

A model based on the concentrated-solution theory was developed for solid electrolytes that accommodate two mobile charge carriers, and used to study lithium and proton mobility in lithium lanthanum niobium oxide materials where some lithium has been replaced by protons, with global stoichiometry $L_{1-y}H_yLNO$. We formulated and solved a non-electroneutral model to elucidate lithium and proton transport, both in diffuse double layers and the neutral bulk, to simulate electrolyte slabs subjected to faradaic currents. A coupled momentum balance was considered to account for stresses that arise due to space charging. The incorporation of a carrier/carrier interaction strength took account of diffusional interactions between lithium ions and protons in a thermodynamically consistent way.

The full non-electroneutral model was solved numerically to describe single-crystal $L_{1-y}H_yLNO$ materials with typical interfacial impedances operated at moderate current density. Substantial stress builds up near the interfaces in response to the development of interfacial space-charge domains. When electrolytes are above the scale of 100 nm thick, the double-layer response becomes decoupled from the bulk polarization due to carrier interdiffusion and migration. For electrolyte slabs in a practical thickness range (> 1 μm), the minimum lithium content is controlled by bulk diffusion; lithium concentration reaches a minimum about 10 Debye lengths from the cathode. In all cases, higher global proton content led to more polarized distributions of both carriers at a given current.

For galvanostatic steady-state carrier distributions in thicker materials, the model was amenable to analytical solution, producing formulas that show how carriers distribute increasingly nonlinearly as the overall level of lithium replacement rises. The two-carrier system manifests a diffusion-limited current density, dependent on the sample conductivity, global proton content, and thickness, as well as the carrier/carrier interaction strength. The limiting current is higher than typical operating current densities for a slab of thickness L if $L/\kappa < 100$ Ωcm^2. The diffusion-limited current of a 100 μm thick single-crystalline LLNO slab with half of its Li^+ exchanged for protons is about 0.67 mAcm^{-2}, however, which is of the same order as the critical current density that has

been observed in other solid-oxide lithium electrolytes. The limiting current is smaller in thicker or less conductive (e.g., polycrystalline) samples, but always becomes much larger as the proton content falls. If protons are present in trace amounts, despite the high limiting current associated with their presence, current nevertheless drives them to accumulate substantially in a thin boundary layer near the cathode surface. This natural accumulation of secondary carriers under applied current may rationalize various observed modes of long-term degradation in solid lithium-ion conductive electrolytes, such as element segregation and defect agglomeration.

Galvanostatic transients were also studied analytically, to explore the characteristic relaxation time and high-current transition time (Sand's time) for systems subjected to step changes in applied current. The time to reach a steady state was found to be of the order of hours, suggesting that most practical materials of this type will operate in an intrinsically transient, rather than a pseudo-steady, mode. Both diffusion and migration contribute to the transient dynamics. Consequently, the relaxation of solid electrolytes is about twice as fast as would be expected for a purely diffusional process. An expression for Sand's time was developed that applies to $L_{1-y}H_yLNO$ systems polarized at more than twice the limiting current. For a sample with given conductivity and proton fraction, measurement of Sand's time could be a useful route to quantify lithium/proton interaction strengths experimentally. Sand's time was found to be of the order of 1 min for polycrystalline $L_{0.5}H_{0.5}LNO$ polarized at 10 $mA\,cm^{-2}$, suggesting that lithium depletion at the cathode could be a driver of failure for this electrolyte.

Declaration of Competing Interest

The authors declare that they have no known competing financial interests or personal relationships that could have appeared to influence the work reported in this paper.

Credit authorship contribution statement

Guanchen Li: Conceptualization, Methodology, Investigation, Writing - original draft. **Charles W. Monroe:** Conceptualization, Methodology, Investigation, Writing - review & editing, Supervision.

Acknowledgments

This work was supported by the Faraday Institution, within the SOLBAT challenge, grant no. EP/S003053/1.FIRG007, and by the UK Engineering and Physical Sciences Research Council (EPSRC) under grant no. EP/P003532/1.

References

[1] Y. Zhu, X. He, Y. Mo, Origin of outstanding stability in the lithium solid electrolyte materials: insights from thermodynamic analyses based on first-principles calculations, ACS Appl. Mater. Interface. 7 (2015) 23685–23693.
[2] Y. Ren, Y. Shen, Y. Lin, C.W. Nan, Direct observation of lithium dendrites inside garnet-type lithium-ion solid electrolyte, Electrochem. Commun. 57 (2015) 27–30.
[3] J.C. Bachman, S. Muy, A. Grimaud, H.-H. Chang, N. Pour, S.F. Lux, O. Paschos, F. Maglia, S. Lupart, P. Lamp, L. Giordano, Y. Shao-Horn, Inorganic solid-state electrolytes for lithium batteries: mechanisms and properties governing ion conduction, Chem. Rev. 116 (2016) 140–162.
[4] V. Thangadurai, S. Narayanan, D. Pinzaru, Garnet-type solid-state fast Li ion conductors for Li batteries: critical review, Chem. Soc. Rev. 43 (2014) 4714–4727.
[5] R.H. Brugge, A.K.O. Hekselman, A. Cavallaro, F.M. Pesci, R.J. Chater, J.A. Kilner, A. Aguadero, Garnet electrolytes for solid state batteries: visualization of moisture-induced chemical degradation and revealing its impact on the Li-ion dynamics, Chem. Mater. 30 (2018) 3704–3713.
[6] M. Kubicek, A. Wachter-Welzl, D. Rettenwander, R. Wagner, S. Berendts, R. Uecker, G. Amthauer, H. Hutter, J. Fleig, Oxygen vacancies in fast lithium-ion conducting garnets, Chem. Mater. 29 (2017) 7189–7196.
[7] F. Han, A.S. Westover, J. Yue, X. Fan, F. Wang, M. Chi, D.N. Leonard, N.J. Dudney, H. Wang, C. Wang, High electronic conductivity as the origin of lithium dendrite formation within solid electrolytes, Nat. Energy 4 (2019) 187–196.
[8] T. Thompson, S. Yu, L. Williams, R.D. Schmidt, R. Garcia-Mendez, J. Wolfenstine, J.L. Allen, E. Kioupakis, D.J. Siegel, J. Sakamoto, Electrochemical window of the Li-ion solid electrolyte $Li_7La_3Zr_2O_{12}$, ACS Energy Lett. 2 (2017) 462–468.
[9] G. Li, C.W. Monroe, Dendrite nucleation in lithium-conductive ceramics, PCCP 21 (2019) 20354–20359.
[10] P. Goyal, C.W. Monroe, New foundations of Newmans theory for solid electrolytes: thermodynamics and transient balances, J. Electrochem. Soc. 164 (2017) E3647–E3660.
[11] J.O. Hirschfelder, R.B. Bird, C.F. Curtiss, Molecular theory of gases and liquids, Wiley, New York, 1964.
[12] C.W. Monroe, C. Delacourt, Continuum transport laws for locally non-neutral concentrated electrolytes, Electrochim. Acta 114 (2013) 649–657.
[13] L. Truong, M. Howard, O. Clemens, K.S. Knight, P.R. Slater, V. Thangadurai, Facile proton conduction in H^+/Li^+ ion-exchanged garnet-type fast Li-ion conducting $Li_5La_3Nb_2O_{12}$, J. Mater. Chem. A 1 (2013) 13469–13475.
[14] F. Fornasiero, J.M. Prausnitz, C.J. Radke, Multicomponent diffusion in highly asymmetric systems. an extended Maxwell–Stefan model for starkly different-sized, segment-accessible chain molecules, Macromolecules 38 (2005) 1364–1370.
[15] S. Yu, R.D. Schmidt, R. Garcia-Mendez, E. Herbert, N.J. Dudney, J.B. Wolfenstine, J. Sakamoto, D.J. Siegel, Elastic properties of the solid electrolyte $Li_7La_3Zr_2O_{12}$(LLZO), Chem. Mater. 28 (2016) 197–206.
[16] L.E. Malvern, Introduction to the mechanics of a continuous medium, Prentice-Hall, New Jersey, 1969.
[17] C.W. Monroe, Mechanics of the ideal double-layer capacitor, J. Electrochem. Soc. 167 (2020) 013550.
[18] A. Sharafi, H.M. Meyer, J. Nanda, J. Wolfenstine, J. Sakamoto, Characterizing the $LiLi_7La_3Zr_2O_{12}$ interface stability and kinetics as a function of temperature and current density, J. Power Source. 302 (2016) 135–139.
[19] T. Swamy, R. Park, B.W. Sheldon, D. Rettenwander, L. Porz, S. Berendts, R. Uecker, W.C. Carter, Y.M. Chiang, Lithium metal penetration induced by electrodeposition through solid electrolytes: example in single-crystal $Li_6La_3ZrTaO_{12}$ garnet, J. Electrochem. Soc. 165 (2018) A3648–A3655.
[20] Z. Ning, D.S. Jolly, G. Li, R. De Meyere, S. Pu, Y. Chen, J. Kasemchainan, J. Ihli, C. Gong, B. Liu, D. Melvin, A. Bonnin, O. Magdysyuk, P. Adamson, G. Hartley, C. Monroe, T. Marrow, P. Bruce, Visualizing plating-induced cracking in lithium anode solid electrolyte cells, Nat. Mater. (2021).
[21] L. Stolz, G. Homann, M. Winter, J. Kasnatscheew, Area oversizing of lithium metal electrodes in solid-state batteries: relevance for overvoltage and thus performance? ChemSusChem 14 (2021) 1–8.
[22] M. Xu, M.S. Park, J.M. Lee, T.Y. Kim, Y.S. Park, E. Ma, Mechanisms of Li^+ transport in garnet-type cubic $Li_{3+x}La_3M_2O_{12}$ (M = Te, Nb, Zr), Phys. Rev. B 85 (2012) 052301.
[23] D. Mazza, Remarks on a ternary phase in the $La_2O_3\square Me_2O_5\square Li_2O$ system (Me = Nb, Ta), Mater. Lett. 7 (1988) 205–207.
[24] G. Li, C.W. Monroe, Modeling lithium transport and electrodeposition in ionic-liquid based electrolytes, Front. Energy Res. 9 (2021) 660081.
[25] Z. Deng, Z. Wang, I.-H. Chu, J. Luo, S.P. Ong, Elastic properties of alkali superionic conductor electrolytes from first principles calculations, J. Electrochem. Soc. 163 (2016) A67–A74.
[26] M.M. Ahmad, Enhanced lithium ionic conductivity and study of the relaxation and giant dielectric properties of spark plasma sintered $Li_5La_3Nb_2O_{12}$ nanomaterials, Ceram. Int. 41 (2015) 6398–6408.
[27] P. Zhao, Y. Xiang, Y. Xu, Y. Wen, W. Zhang, X. Zhu, M. Li, S. Zhang, H. Ming, Z. Jin, G. Cao, Dense garnet-like $Li_5La_3Nb_2O_{12}$ solid electrolyte prepared by self-consolidation method, J. Power Source. 388 (2018) 25–31.
[28] C. Galven, J.-L. Fourquet, M.-P. Crosnier-Lopez, F.L. Berre, Instability of the lithium garnet $Li_7La_3Sn_2O_{12}$: Li^+/H^+ exchange and structural study, Chem. Mater. 23 (2011) 1892–1900.
[29] C. Galven, J. Dittmer, E. Suard, F.L. Berre, M.P. Crosnier-Lopez, Instability of lithium garnets against moisture. structural characterization and dynamics of $Li_{7-x}H_xLa_3Sn_2O_{12}$ and $Li_{5-x}H_xLa_3Nb_2O_{12}$, Chem. Mater. 24 (2012) 3335–3345.
[30] R. Malik, D. Burch, M. Bazant, G. Ceder, Particle size dependence of the ionic diffusivity, Nano Lett. 10 (2010) 4123–4127.
[31] D.M. Pesko, K. Timachova, R. Bhattacharya, M.C. Smith, I. Villaluenga, J. Newman, N.P. Balsara, Negative transference numbers in poly(ethylene oxide)-based electrolytes, J. Electrochem. Soc. 164 (2017) E3569–E3575.
[32] W.G. Zeier, Structural limitations for optimizing garnet-type solid electrolytes: a perspective, D top Dalton Trans. 43 (2014) 16133–16138.
[33] D. Rettenwander, G. Redhammer, F. Preishuber-Pflügl, L. Cheng, L. Miara, R. Wagner, A. Welzl, E. Suard, M.M. Doeff, M. Wilkening, J. Fleig, G. Amthauer, Structural and electrochemical consequences of al and ga cosubstitution in $Li_7La_3Zr_2O_{12}$ solid electrolytes, Chem. Mater. 28 (2016) 2384–2392.
[34] F. Pesci, R.H. Brugge, A.K.O. Hekselman, A. Cavallaro, R.J. Chater, A. Aguadero, Elucidating the role of dopants in the critical current density for dendrite formation in garnet electrolytes, J. Mater. Chem. A 6 (2018) 19817–19827.
[35] L. Cheng, W. Chen, M. Kunz, K. Persson, N. Tamura, G. Chen, M. Doeff, Effect of surface microstructure on electrochemical performance of garnet solid electrolytes, ACS Appl. Mater. Interface. 7 (2015) 2073–2081.
[36] F. Flatscher, M. Philipp, S. Ganschow, H.M.R. Wilkening, D. Rettenwander, The

natural critical current density limit for $Li_7La_3Zr_2O_{12}$ garnets, J. Mater. Chem. A 8 (2020) 15782–15788.
[37] R. Murugan, V. Thangadurai, W. Weppner, Fast lithium ion conduction in garnet-type $Li_7La_3Zr_2O_{12}$, Angew. Chem. Int. Ed. 46 (2007) 7778–7781.
[38] X. Liu, Y. Chen, Z.D. Hood, C. Ma, S. Yu, A. Sharafi, H. Wang, K. An, J. Sakamoto, D.J. Siegel, Y. Cheng, N.H. Jalarvo, M. Chi, Elucidating the mobility of H^+ and Li^+ ions in $Li_{6.25-x}H_xAl_{0.25}La_3Zr_2O_{12}$ via correlative neutron and electron spectroscopy, Energy Environ. Sci. 12 (2019) 945–951.
[39] J. Liu, C.W. Monroe, On the characterization of battery electrolytes with polarization cells, Electrochim. Acta 167 (2015) 357–363.
[40] M. Abramowitz, I.A. Stegun (Eds.), Handbook of Mathematical Functions with Formulas, Graphs, and Mathematical Tables, National Bureau of Standards, 1972. ed. 10
[41] R.J.-Y. Park, C.M. Eschler, C.D. Fincher, A.F. Badel, P. Guan, M. Pharr, B.W. Sheldon, W.C. Carter, V. Viswanathan, Y.M. Chiang, Semi-solid alkali metal electrodes enabling high critical current densities in solid electrolyte batteries, Nat. Energy (2021) 314–322.